Hindawi
Structural Control and Health Monitoring
Volume 2024, Article ID 6896975, 20 pages
https://doi.org/10.1155/2024/6896975

Research Article

Damage Identification Method of Tied-Arch Bridges Based on the Equivalent Thrust-Influenced Line

Yu Zhou,[1,2,3] **Meng Li**,[1] **Yingdi Shi**,[1] **Shengkui Di**,[2] **and Xianzeng Shi**[1]

[1]*College of Civil Engineering, Anhui Jianzhu University, Hefei 230601, China*
[2]*School of Civil Engineering, Lanzhou Jiaotong University, Lanzhou 730070, China*
[3]*National and Local Joint Engineering Laboratory of Building Health Monitoring and Disaster Prevention Technology, Anhui Jianzhu University, Hefei 230601, China*

Correspondence should be addressed to Yu Zhou; yuzhou923@outlook.com

Received 26 September 2023; Revised 8 December 2023; Accepted 28 December 2023; Published 9 January 2024

Academic Editor: Suparno Mukhopadhyay

Early tied-arch bridges cannot satisfy the current traffic load demand due to their load grades and maintenance levels. Also, these tied-arch bridges have accumulated structural damage with increasingly prominent safety risks. In order to accurately evaluate the characteristics of tied-arch bridges' structural-influenced lines and identify damage of their arch ribs and suspenders, two analytical solutions are derived and established in this paper for the thrust-influenced lines of parabola and catenary two-hinged arches with a tie beam. A new method and an index for identifying damage of arch ribs and suspenders of tied-arch bridges are proposed. The results of numerical simulation in this paper verified that the proposed analytical solution has good analytical accuracy in practice on those two-hinged nonflat arches. With the use of equivalent thrust-influenced line difference curvature, the effectiveness of damage identification and the verification method were verified on the tie beam, suspender, and arch rib of plane tie arch structure as well as the suspender and arch rib of tied-arch bridges in this research. Furthermore, combining with grey relation analysis, the noise immunity of the proposed index method can be verified. Also, thrust-influenced line recognition based on VMD (variational mode decomposition) is introduced, and a practical process of bridge health assessment based on the quasistatic-influenced line loading of three-axle heavy vehicles is established. Theoretical analysis and numerical verification show that the calculated error of the analytic solution of two-hinged arches with a rise-span ratio greater than 1/8 is less than 9.57%, and the error decreases with the increase of the rise-span ratio. Therefore, it can be applied to the calculation and analysis of tied-arch bridges with a rise-span ratio range between 1/4 and 1/5. With the equivalent thrust-influenced line index proposed in this paper, the damage of suspenders and arch ribs of tied-arch bridges can be accurately located. It has been found that the proposed method is more effective to identify the damage of suspenders than the damage of arch ribs does, showing good noise immunity. In summary, this research has provided theoretical support for arch bridge design and evaluation. Combining with existing bridge-monitoring methods, the new bridge damage identification method proposed in this paper has the prospect of realizing the normal health status assessment of existing tied-arch bridges.

1. Introduction

As one of the most common bridge types in China [1], the arch bridge presents reasonable structural forces and a beautiful shape [2, 3]. With the increasingly mature analysis theory of arch bridges [4], tied-arch bridges are widely used due to their characteristics of an explicit force transmission path and large span capacity [5, 6]. In terms of structural stress, tied-arch bridges have a two-hinged main arch structure, with horizontal thrust at the arch foot withstood by the tie beam and no horizontal external force generated at the arch foot [7]. Therefore, uneven settlement of the pier will have less influence on the internal force distribution of the structure, which has a stronger capacity to fit with the terrain. However, in recent years, accidents of through tied-arch bridges and half-through tied-arch bridges have occurred frequently and commonly and the failure of main components (such as suspenders and arch

ribs) will bring about changes in the force transmission paths, thus resulting in structural instability and damage [8]. Meanwhile, arch ribs and suspenders, as the main stressed components in the tied-arch bridge structural system, comprise the main paths for bridge decks-transmitting loading and once they are severely damaged, major structural safety accidents will occur [9].

In the face of the increasing number of arch bridge accidents, domestic and international scholars have carried out many useful scientific studies [10]. Civera et al. [11] tested and validated a novel multistage clustering algorithm for SHM applications of automatic OMA (AOMA), especially for damage detection and severity assessment of masonry arch bridges. Ge et al. [12] presented an experimental validation for a high-precision vision-based displacement-influenced line (DIL) measurement system for the purpose of damage detection on bridges. Lonetti et al. [13] proposed a numerical investigation to identify the instability strength of tied-arch bridges due to vertical loads. Bozyigit et al. [14] proposed a dynamic stiffness method- (DSM-) based practical approach is developed to calculate vibration frequencies and mode shapes of masonry arch bridges. Chen et al. [15] proposed a quantification method of structural damage by reconstructing the deflection-influenced line matrix using the matrix decomposition method, revealing the relationship between structural damage and change in the deflection-influenced line. Fan et al. [16] proposed an identification method for the damage of displacement difference-influenced lines of tied-arch bridges, derived the displacement-influenced lines of tied-arch bridges with the force method equation, and verified the effectiveness of those displacement difference-influenced lines derived in identifying the suspender damage of arch bridges through the finite element model. Breccolotti and Natalicchi [17] proposed a bridge damage identification method with bridge deflection, corner-influenced line, and dynamic weighing system combined. Zhu et al. [18] proposed a damage identification method for long-span bridges based on the strain-influenced line and information fusion. Based on the main analytical parameters of extreme events and limit states of tie beam failure, Fan et al. [19] proposed a robustness evaluation framework for tie beam failure, which can be used to evaluate the safety of in-service bridges. Based on the convolutional neural network, Duan et al. [20] proposed a damage identification method for tied-arch bridge suspenders, with its robustness having been proved in various noise environments. Based on the Ritz method, Feng et al. [21] introduced the Hellinger–Reissner variational theory to improve the rapid decision-making approximation solution for parameters of tied-arch bridges and used this theory in the deformation and force analysis of tied-arch bridges for the first time. These existing studies have provided theoretical support and a method reference for the damaged calculation and health assessment of arch bridge structures and further revealed the explicit analytical relationship between damage of tied-arch bridges and important mechanical indices, thus providing an important way for scientifically evaluating the damage status of tied-arch bridges' components. This paper has proposed an accurate method for identifying the damage of the main stressed components of tied-arch bridges, thus providing a solution for this key scientific problem in structural health assessment of bridges.

Because horizontal thrust at the arch feet of tied-arch bridges is balanced by tie beams [22], arch ribs serve to offset the horizontal thrust through the tension previously exerted by tie beams, so that supports at arch feet will not produce horizontal external force. Under such a circumstance, the influence line of tie beams' axial force, which is easy to test in practice, can be viewed as the equivalent thrust-influenced line (ETIL). In the current research, the influence line is a perfect parameter for assessing the health status of tied-arch bridges [23]. In view of this, with the force method equation, two analytical solutions of the axial force-influenced line of the two-hinged arch tie beam with the variable section are derived in this paper. That is, such parameters as the equivalent thrust-influenced line, explicit expression of damage, and ETIL of tied-arch bridges are established in this paper, with a new damage identification index of equivalent thrust-influenced line difference curvature (ETILDC) proposed. Furthermore, through numerical simulation, the accuracy of the inferred analytical solution is evaluated, with its application feasibility of damage identification studied. In summary, this paper has provided theoretical support and an ideal reference for design calculation and health assessment of tied-arch bridges.

2. The Establishment of Analytical Solution

2.1. Theoretical Basis. As one of the main stressed components of a tied-arch bridge, the arch rib has a typical two-hinged arch structure with variable sections. Figure 1 shows the mechanical calculation the model of the arch rib. F_P is the unit moving load. The arch axis equations for the parabola and catenary variable sections of the two-hinged arch (equations (1) and (2)) [24] and the calculation formula for the arch-axis geometric parameter k are equations (3) and (4) [24] are as follows.

$$y = \frac{\left(4\mathrm{fx}^2\right)}{(2L)^2}, \tag{1}$$

$$y = f\,\frac{(\cos h\,\mathrm{kx}/L - 1)}{(m-1)}, \tag{2}$$

$$k = \ln\left(m + \sqrt{m^2 - 1}\right), \tag{3}$$

$$m = \frac{g_j}{g_d}, \tag{4}$$

where L represents the half-span of the two-hinged arch, f is the vector height, m is the arch coefficient (g_j is constant load strength at the arch foot and g_d is constant load strength at the arch vault), and x is the horizontal distance from any section of the arch to the arch vault.

Arch sections can be set based on Ritter's formula (equations (5) and (6)) [24], and the variable cross-section heights of two arch-axis types can be calculated with equations (7) and (8).

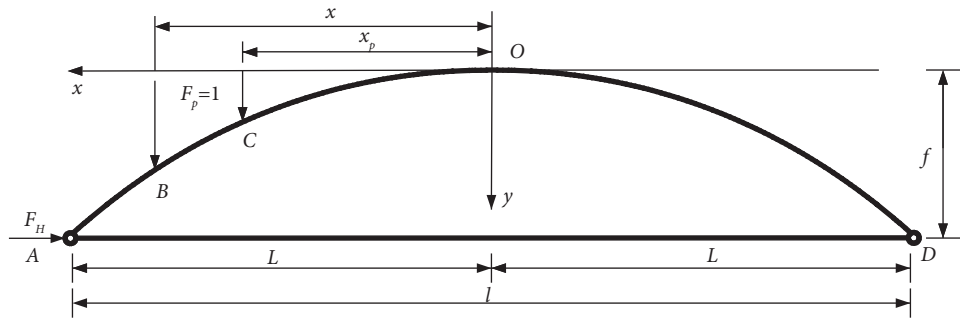

Figure 1: Mechanical model of two-hinged tied-arch structure.

$$I = \frac{I_0}{[(1 - x/L + \mathrm{nx}/L)\cos\varphi]}, \tag{5}$$

$$A = A_0\left[\left[1 - \frac{(1-n)x}{L}\right]\cos\varphi\right]^{-1/3}. \tag{6}$$

The height of the parabola axis is as follows:

$$h = \left\{\frac{h_0\left(4f^2x^2 + L^4\right)^{1/2}}{(L^2 - \mathrm{xL} + \mathrm{nxL})}\right\}^{1/3}. \tag{7}$$

The height of the catenary axis is as follows:

$$h = \left\{\frac{\left[h_0^3\left(1 + \left(k^2f^2(\sin \mathrm{hkx}/L)^2\right)/\left((m-1)^2 - L^2\right)\right)^{1/2}\right]}{(1 - x/L + \mathrm{nx}/L)}\right\}^{1/3}, \tag{8}$$

where n is the coefficient of change in the arch rib section, φ is the horizontal angle of the arch section, I_0 and h_0 are the moments of inertia of the arch vault and height of the arch vault section, respectively, and A_0 is the cross-sectional area of the arch rib vault position.

2.2. Derivation of Analytical Solution. The superfluous constraint along the horizontal direction at the arch foot is replaced by redundant force F_H. F_H represents both the thrust at the two-hinged arch feet and the tie beam axis force of the two-hinged arch, as shown in Figure 1.

The upper arch ribs of two-hinged arches with and without tie beam have the same form. However, tie beam deformation needs to be considered when the δ_{11} parameter of the two-hinged arch structure with the tie beam is calculated with equations (9) and (25).

The flexibility coefficient is as follows:

$$\delta_{11} = \int_s \frac{M_1^2}{EI}\mathrm{d}s + \int_s \frac{N_1^2}{EA}\mathrm{d}s + \frac{l}{E^*A^*}. \tag{9}$$

The displacement equation is as follows [25]:

$$\Delta_{1p} = \int_s \frac{M_1M_p}{EI}\mathrm{d}s, \tag{10}$$

where Δ_{1p} is the displacement of the basic structure (Figure 1) in the direction F_H under the action of the load alone, E is the elastic modulus of the arch rib, E^* is the elastic modulus of the tie beam, A^* is the tie beam section area, and l is the tie beam length ($l = 2L$).

The bending moment equation is as follows:

$$M_1 = -(f - y). \tag{11}$$

The axial force equation is as follows:

$$N_1 = -\cos\varphi. \tag{12}$$

The bending moment equations are as follows.

When $-L < x < x_p$,

$$M_P = \left(\frac{1}{2} - \frac{x_p}{2L}\right)(L + x). \tag{13}$$

When $x_p < x < L$,

$$M_P = \left(\frac{x_p}{2L} + \frac{1}{2}\right)(L - x). \tag{14}$$

The elastic displacement at any point subjected to the load can be simplified according to the displacement reciprocity theorem and virtual work principle of deformation as follows:

$$\Delta = \left(\sum\int \frac{\overline{M}M_p}{\mathrm{EI}} + \sum\int \frac{\overline{F}F_p}{\mathrm{EA}} + \sum\int \frac{k\overline{Q}Q_p}{\mathrm{GI}}\right)\mathrm{d}s \approx \sum\int \frac{\overline{M}M_p}{\mathrm{EI}}\mathrm{d}s, \tag{15}$$

where Δ is the deformation displacement; EI, EA, and GA are the beam section's bending, tensile, and shear stiffness, respectively; and M, F, and Q represent the bending moment, axial force, and shear force, respectively. The three integral functions represent bending deformation, axial deformation, and shear deformation, respectively.

Therefore, in order to facilitate the analytical calculation, the axial deformation of arch ribs is not considered in the derivation, with only the axial deformation of tie beams considered (equation (16)).

$$\delta_{11} = \int_s \frac{M_1^2}{\mathrm{EI}} \mathrm{d}s + \frac{2L}{E^* A^*}. \tag{16}$$

The flexibility coefficient equation is as follows:

$$\delta_{11} = \int_{-L}^{L} \frac{(f-y)^2}{\mathrm{EI}\cos\varphi} \mathrm{d}x + \frac{2L}{E^* A^*}. \tag{17}$$

The displacement equation is as follows:

$$\Delta_{1p} = \int_{-L}^{x_p} \frac{\left((1/2) - \left(x_p/2L\right)\right)(L+x)(y-f)}{\mathrm{EI}\cos\varphi} \mathrm{d}x + \int_{x_p}^{L} \frac{\left(\left(x_p/2L\right) + (1/2)\right)(L-x)(y-f)}{\mathrm{EI}\cos\varphi} \mathrm{d}x, \tag{18}$$

where x_p is the load action position, y is the mathematical expression of the arch axis, φ is the horizontal angle of the arch section, and x is the horizontal distance from any section of the arch structure to the arch vault.

With the fitting method expressed in equations (19) and (25), the parabola and catenary fitting formulas (equations (20) and (21)) can be obtained through equations (1) and (2).

$$\mathrm{d}s = \frac{1}{\cos\varphi \mathrm{d}x}. \tag{19}$$

The parabola fitting formula is as follows:

$$\cos\varphi = \frac{L^2}{\left(L^4 + 4f^2x^2\right)^{1/2}}. \tag{20}$$

The catenary fitting formula is as follows:

$$\cos\varphi = \left[1 + \frac{k^2 f^2 (\sinh kx/L)^2}{(m-1)^2 L^2}\right]^{-1/2}. \tag{21}$$

The thrust-influenced line expression formula is as follows:

$$F_H = \frac{-\Delta_{1P}}{\delta_{11}}. \tag{22}$$

With equations (1)–(5) and (20) and (21) substituted into equations (17) and (18), the analytical expression of redundancy force for the tie beam with two-hinges arch can be obtained, as shown in Table 1. With equations (1), (2), (17), and (18) substituted into equation (22), the analytical solution of the tie beam axial force-influenced line on the two-hinged arch of the tie beam is obtained. The ETIL analytical solution for the tie beam with two-hinged arch can be obtained, as shown in Table 2.

2.3. Accuracy Analysis of Analytical Solution. With the MIDAS/Civil finite element software, a model of two-hinged arch ribs with the parabola and catenary tie beam is established in this paper, with the five rise-span ratios of 1/4, 1/5, 1/6, 1/7, and 1/8 applied. Linear-elastic material behavior in the finite element model is assumed [26]. The parameters of this arch rib model are as follows.

The span diameter is 50.934 m, the vault section size is 1 m × 1 m, and the tie beam section size is 1 m × 1 m. C40 is used as the material of the arch rib. The elastic modulus of C40 concrete is $3.25e+07$ kN/m^2, the Poisson ratio of C40 concrete is 0.2, the volumetric weight is 25 kN/m^3, and the coefficient of linear expansion of C40 concrete is $1.20e-05$ (1/°C). C50 is used as the material of the tie beam. The elastic modulus of C50 concrete is $3.45e+07$ kN/m^2, the Poisson ratio of C50 concrete is 0.2, the volumetric weight is 25 kN/m^3, and the coefficient of linear expansion of C50 concrete is $1.0e-05$ (1/°C).

Also, the arch rib variable sections of this model can be determined using equations (7) and (8).

This finite element model has a total of 158 nodes and 158 elements, with its tie beam structure divided into 108 beam elements and a tie beam element length of 1.01868 m, as shown in Figure 2. In this finite element model, the arch rib is loaded with a quasistatic-influenced line, with a total of 109 times of loading with a loading step of 0.5 m. To make the model as close to reality as possible, the software does not ignore the axial deformation and shear deformation of the arch rib. In this paper, the ETIL at the 1# measurement location of the arch rib can be extracted. Figure 3 shows the ETIL curve of the two-hinged arch with the tie beam drawn with the horizontal distance of the unit force application position from the arch vault viewed as an independent variable and the influence line coefficient viewed as a dependent variable.

From Figure 3, it can be seen that the analytical value of the ETIL with the tie beam is less than that without the tie beam and the parabola with the tie beam is close to the amplitude of the ETIL of the two-hinged arch of the catenary with the tie beam. Based on equations (17) and (22), it can be seen that when the elastic modulus of the tie beam is greater than that of the arch rib, the analytical solution presents basically equal values on the tie beam, with similar force states obtained. Assume that the numerical solution presents a true value of S and the analytical solution presents an approximate value of $\overline{S}$, then the relative error $\widetilde{S}$ can be calculated with (23). With the two curve sets ((a)–(e) and (f)–(j)) presented in Figure 3 substituted into equation (23), it can be calculated that the maximum relative errors of parabola and catenary two-hinged arches with tie beam are 10.29% under different rise-span ratios (and under a 1/8 rise-

Table 1: Analytical expression of redundancy force.

Displacements	Parabola	Catenary
δ_{11}	$16f^2L/15EI_0 + 2L/E^*A^*$	$[f^2L/4kEI_0(m^2 - 2m + 1)](8km^2 + 8e^{-k}m - 8e^km - e^{-2k} + e^{2k} + 4k) + 2L/E^*A^*$
Δ_{1p}	$[-5f(L + x_p)(L - x_p)/12L^3EI_0][3x_p^3(1 - n)/25 - Lx_p^2/5 + 7L^2(n - 1)x_p/25 + L^3]$	$-f/2Lk^3EI_0(m - 1)\{[(k + 2n - 2)L + kx_p(n - 1)]L^2e^{-kx_p/L} - [(k - 2n + n)L + kx_p(n - 1)]L^2e^{kx_p/L} + [kL + x_p(n - 1)(k + 2)]L^2e^{-k} + [kL + x_p(n - 1)(k - 2)]L^2e^k - k^3m(L - x_p)(x_p + L)(L + nx_p/3 - x_p/3)\}$

Table 2: Practical analytical solution of the equivalent thrust-influenced line.

Parabola	Catenary
$f(7nx_pL^2 - 3nx_p^3 + 25L^3 - 7x_pL^2 - 5x_p^2L + 3x_p^3)(L^2 - x_p^2)E^*A^*/(64f^2E^*A^* + 120EI_0)L^4$	$f\{[(k + 2n - 2)L + kx_p(n - 1)]L^2e^{-kx_p/L} + L^2e^{kx_p/L}[(k2n + 2)L + kx_p(n - 1)] - L^2e^{-k}[kL + x_p(n - 1)(k + 2)] - [kL + x_p(n - 1)(k - 2)]L^2e^k + k^3m(L - x_p)(L + x_p)(L + nx_p/3 - x_p/3)\}/\{2Lk^3(m - 1)EI_0[f^2L(8km^2 + 8e^{-k}m - 8e^km - e^{-2k} + e^{2k} + 4k)/4kEI_0(m^2 - 2m + 1) + 2L/E^*A^*]\}$

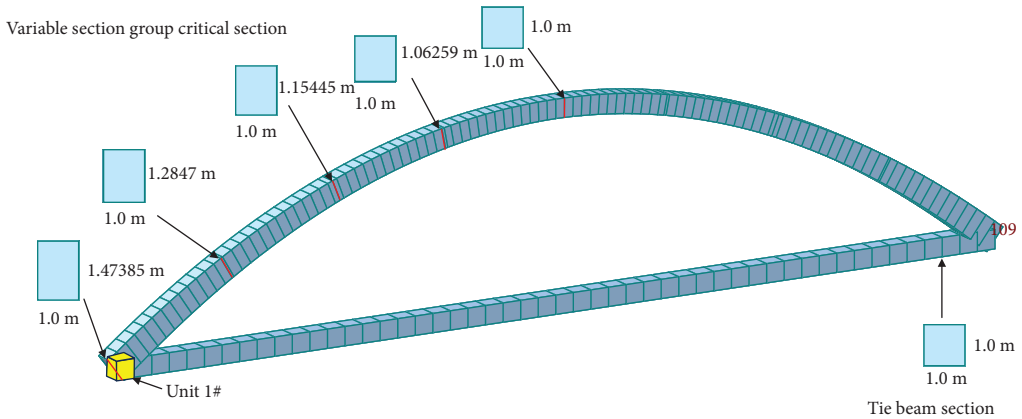

Figure 2: Finite element model of two-hinged arch rib with the tie beam.

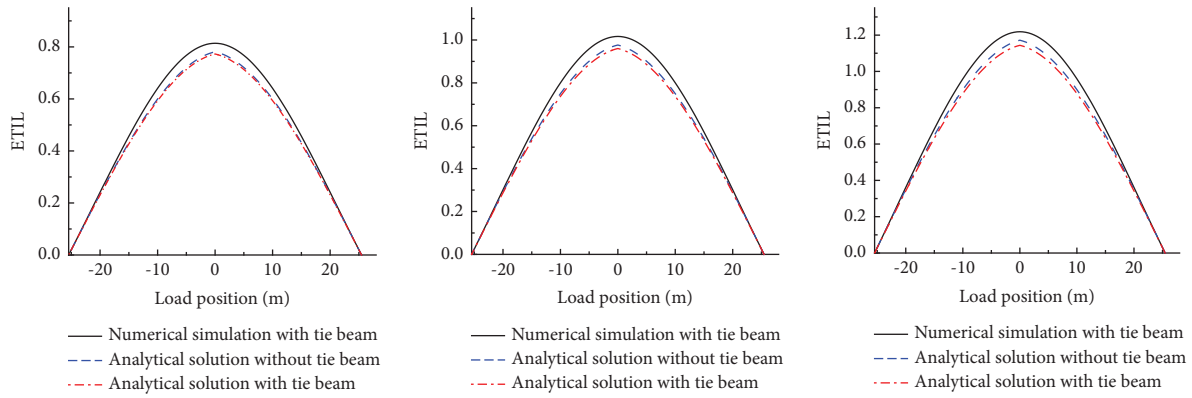

Figure 3: Continued.

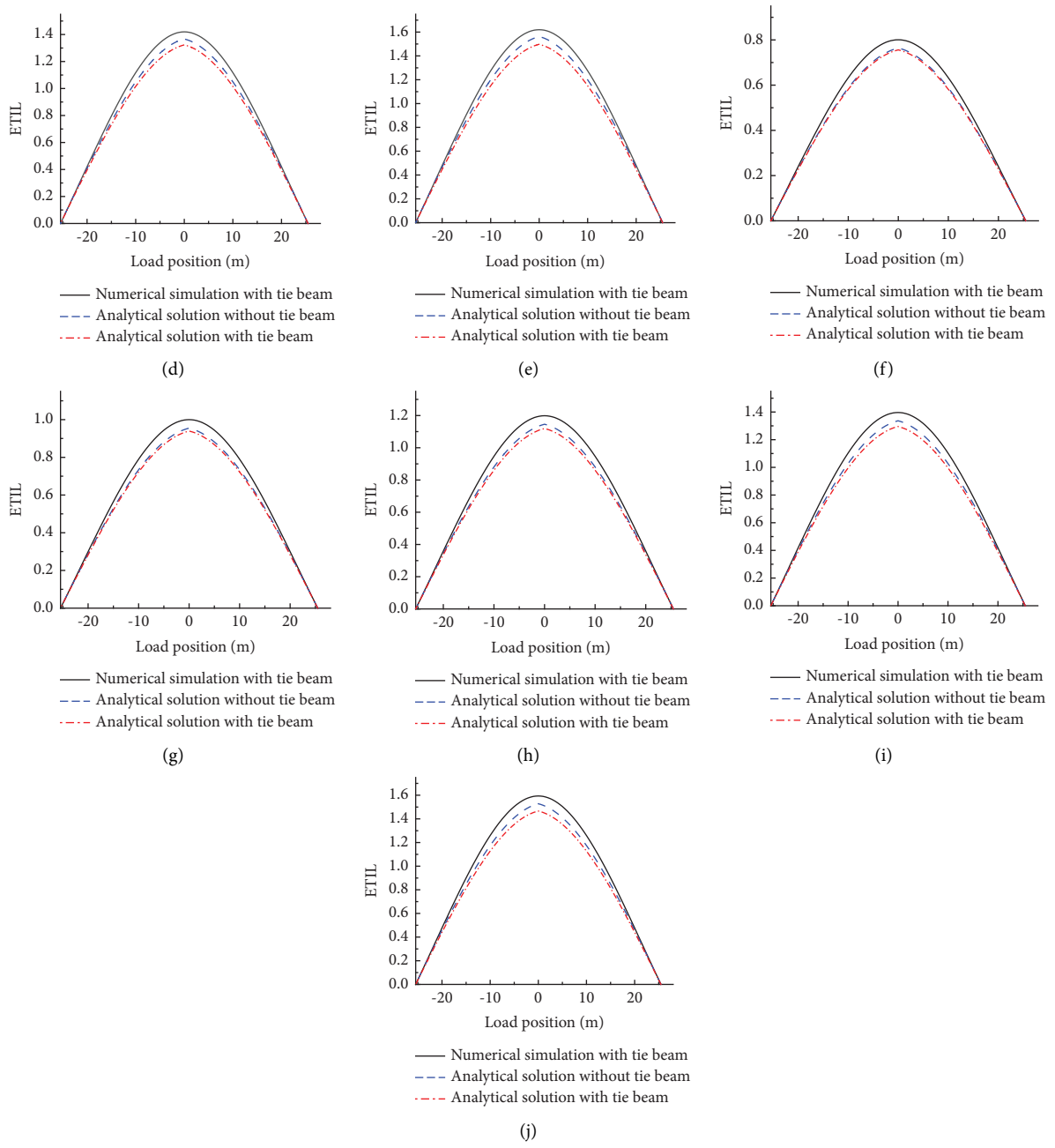

Figure 3: Comparison of numerical simulation and analysis results of ETIL of two-hinged arches with the tie beam. (a) Parabola tied-arch structure with the 1/4 rise-span ratio. (b) Parabola tied-arch structure with the 1/5 rise-span ratio. (c) Parabola tied-arch structure with the 1/6 rise-span ratio. (d) Parabola tied-arch structure with the 1/7 rise-span ratio. (e) Parabola tied-arch structure with the 1/8 rise-span ratio. (f) Catenary tied-arch structure with the 1/4 rise-span ratio. (g) Catenary tied-arch structure with the 1/5 rise-span ratio. (h) Catenary tied-arch structure with the 1/6 rise-span ratio. (i) Catenary tied-arch structure with the 1/7 rise-span ratio. (j) Catenary tied-arch structure with the 1/8 rise-span ratio.

span ratio of catenary two-hinged arch with the tie beam) and it can also be seen that with the decrease in the rise-span ratio, the difference between the finite element analysis results of numerical simulation and analytical solution gradually increases. Besides their bending deformation, the axial deformation of flat arches with a rise-span ratio less than 1/5 should not be overlooked. Therefore, the analytical solution of ETIL of two-hinged arches with tie beams can present more accurate results on those steep-arch structures with a rise-span ratio greater than 1/5. As shown in Table 3, the relative errors between numerical simulation and analytical solution of the critical section ETIL of two-hinged arches with tie beams are negatively correlated with their rise-span ratios.

Table 3: Comparison between results of analytical calculation and finite element numerical simulation.

Rise-span ratios	Loading position of load action x_p	Parabola			Catenary		
		Analytical solution (kN)	Numerical simulation (kN)	Relative error (%)	Analytical solution (kN)	Numerical simulation (kN)	Relative error %
1/4	$\pm l/8$	0.267743717	0.28108	4.744657286	0.263268143	0.27935	5.75688441
	$\pm 2l/8$	0.50717042	0.545606	7.044566995	0.497410777	0.539688	7.833641493
	$\pm 3l/8$	0.685857426	0.740079	7.326457554	0.671220943	0.729135	7.942844261
	$4l/8$	0.772831115	0.813924	5.048737302	0.755961929	0.800645	5.580884287
1/5	$\pm l/8$	0.332663177	0.350976	5.217685397	0.327175921	0.348843	6.211126151
	$\pm 2l/8$	0.63014335	0.681321	7.511532772	0.618156178	0.673971	8.28148726
	$\pm 3l/8$	0.852156355	0.924258	7.801030113	0.834158388	0.910603	8.39494401
	$4l/8$	0.960218438	1.016533	5.539865632	0.939470068	0.999931	6.046510459
1/6	$\pm l/8$	0.396277631	0.420664	5.797113444	0.389846709	0.418134	6.765125869
	$\pm 2l/8$	0.750644289	0.816622	8.079345266	0.736564447	0.807851	8.824220494
	$\pm 3l/8$	1.015112357	1.107853	8.371204754	0.993942039	1.091504	8.938305448
	$4l/8$	1.143838917	1.218483	6.12598477	1.119426248	1.198584	6.604272375
1/7	$\pm l/8$	0.458363974	0.490094	6.474273548	0.451067715	0.487177	7.41194379
	$\pm 2l/8$	0.868250622	0.951422	8.741796816	0.852233543	0.941245	9.456778788
	$\pm 3l/8$	1.174153921	1.290756	9.033626727	1.150029368	1.271737	9.570188805
	$4l/8$	1.323048567	1.419668	6.805776632	1.29521945	1.396498	7.252323312
1/8	$\pm l/8$	0.518718049	0.559225	7.243408413	0.510643509	0.555928	8.145747561
	$\pm 2l/8$	0.982575627	1.085634	9.492920561	0.964794226	1.074072	10.17415723
	$\pm 3l/8$	1.328758075	1.472856	9.78357185	1.301922112	1.451198	10.28639014
	$4l/8$	1.497258098	1.619964	7.57460672	1.466288503	1.593562	7.986730168

Note. The load action position refers to the loading position on the critical section of arch structure.

$$\widetilde{S} = \frac{\Delta S}{S} \times 100\% = \frac{|S - \overline{S}|}{S} \times 100\%. \quad (23)$$

According to Table 3, the relative errors between the ETIL analytical solution and ETIL numerical simulation of the critical section of two-hinged arches with tie beams increase with the decrease in arch rise-span ratio, with a maximum relative error of 9.57% under an arch rise-span ratio of 1/7. Therefore, the ETIL analytical solution of the critical section of two-hinged arches with tie beams is applicable for evaluating parabola and catenary two-hinged arch structures with tie beams under a rise-span ratio greater than 1/7. Figure 4 presents the patterns of these relative errors. It can be seen that in the $4l/8$ and $l/8$ sections of these arch structures, there appear the smallest relative errors between the ETIL analytical solution and ETIL numerical simulation. Among those arches with five different rise-span ratios, there are the largest relative errors between the ETIL analytical solution and ETIL numerical simulation on the critical sections of two-hinged arches with tie beams under a rise-span ratio of 1/8.

3. Finite Element Simulation Verification

3.1. Damage Identification Method of Planar Tied-Arch Structures. Concerning the ETIL analytical solutions of the parabola and catenary arch structures with the tie beam in an undamaged state as shown in Table 2, the elastic modulus at the damaged arch rib is represented by E', the elastic modulus at the damaged tie beam is represented by $E^{*\prime}$, and the ETIL at the damaged state is represented by F_H^*. In the curvature formula, $1/\rho(x_p) = |F_H''|/(1 + F_H'^2)^{3/2}$; the first derivative of thrust F_H is approximately equal to zero. Therefore, this formula can be simplified to the following formula: $1/\rho(x_p) = |F_H''|$. So, the formula of ETILDC before and after damage can be written as $1/\rho(x_p) = |(F_H - F_H^*)''|$. When the load moves to the damaged region, $(F_H - F_H^*)''$ is not equal to zero, leading to an abrupt change in the curve. It proves that the ETILDC can be used for locating bridge damage.

From Table 4, it can be seen that values of ETILDC in all damaged sections are not equal to zero, which indicates the feasibility of locating the damage of the stressed components of the planar tied-arch structures by ETILDC. The appearance of the suspenders makes the force transmission path of the planar tied-arch system clear; theoretically, the damage of the suspenders can be reflected by ETILDC. In order to perform research on the effectiveness of the ETILDC index in identifying damage to planar tied-arches, a planar tied-arch model with suspenders is established in this paper. In this FE model which is established by MIDAS/Civil software, linear-elastic material behavior is assumed. C50 is used as the material of the arch rib, which has a span of 63.8 m and a vector height of 11.86 m, wherein the elastic modulus of C50 concrete is $3.45e+07\,\text{kN/m}^2$, the Poisson ratio of C50 concrete is 0.2, the volumetric weight is $25\,\text{kN/m}^3$, and the coefficient of linear expansion of C50 concrete is $1.20e-05$ (1/°C). The elastic modulus of the suspender is $2.06e+08\,\text{kN/m}^2$, the Poisson ratio of the suspender is 0.3, the volumetric weight is $76.98\,\text{kN/m}^3$, and the coefficient of linear expansion of the suspender is $1.0e-05$ (1/°C). Quasistatic-influenced line loading is carried out on the beam of the planar tied-arch with suspender in this FE model, as shown in Figure 5. A total of 29 loading steps are set on the 28 units of the tie beam. The cross-sections of the tie beam have the structure of single room box beam, and the preset initial tension of the suspenders is shown in Figure 6. Bozyigit et al. ([27], [28]) had modelled damage as stiffness reduction considering linear rotational spring. In this paper, the damage is simulated with the reduction of the elastic modulus of damaged elements. As shown in Table 5, the damage extent of the midspan arch beam, midspan arch rib, and midspan arch suspender are set as 10%, 30%, and 50%, respectively. Then, the effectiveness of ETILD in identifying and locating planar tied-arch structure damage is investigated in this paper.

As shown in Figure 7, with ETILDC, damage to the midspan arch beam, arch rib, and suspender of the planar tied-arch structure can be well located. When there is the same extent of damage to different stress components in the midspan arch location, ETILDC is more effective in identifying the damage of the tie beam than in identifying the damage of the suspenders. Meanwhile, it is more effective in locating the damage to the suspenders than in locating the damage to the arch rib. The ETILDC curves presented in Figures 7(a)–7(c) show that the damage of the tie beam and suspender is more obvious. Under the same damage extent of different stressed components, there are different ETILDC curve patterns among these stressed components. Therefore, based on the amplitudes and patterns of ETILDC curves, the damage of stressed components of planar tied-arch structure can be roughly judged. This result shows that the ETILDC index effectively identifies the damage of the main stressed components of the planar tied-arch structure.

3.2. Loading Model for Tied-Arch Bridge Damage Identification. In practical engineering, it is difficult to perform direct loading on arch ribs of through tied-arch bridges and half-through tied-arch bridges. In this paper, the axial force-influenced line of the tie beam at the arch foot is equivalent to the thrust-influenced line of the arch foot of the two-hinged arch. Therefore, the ETIL can be obtained by extracting the axial force-influenced line of the unit (unit25#) at the connection between the tie beam and the arch foot. ETIL of the tie beam section (Figure 8, unit 25#) of the tied-arch bridge can be extracted through the loading of moving unit force on the bridge deck, and the effectiveness of ETIL in identifying the damage of the main stressed components of tied-arch bridges are further verified.

In this FE model which is established by MIDAS/Civil software, a tied-arch bridge model with a span of 60 m, a vector height of 12 m, and a total of 11 pairs of suspenders are established and linear-elastic material behavior is assumed,

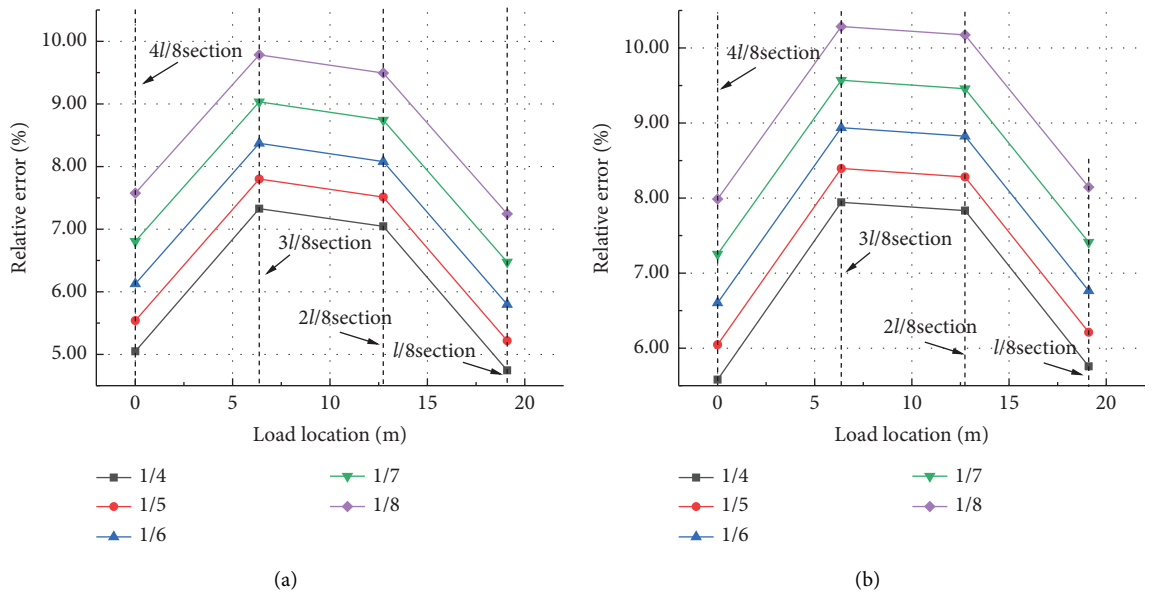

Figure 4: Comparison of relative errors between analytical solution and numerical simulation of the critical sections of two-hinged arches with different arch axis types. (a) Relative errors between analytical solution and numerical simulation of the critical sections of parabola two-hinged arches with the tie beam. (b) Relative errors between analytical solution and numerical simulation of the critical sections of catenary two-hinged arches with the tie beam.

Table 4: Expressions of ETILDC at damage region of arch bridges under two arch-axis types.

	Parabola	Catenary
Arch rib damaged	$225I_0 f A^* E^* (E - E')(L - x_P)(L + x_P)$ $(x_P n + L - x_P)/2L^4 (8f^2 E^* A^* + 15EI_0)$ $(8f^2 E^* A^* + 15E' I_0)$	$d^2\{-aE^* A^* L^2 k^3 I_0 (m-1)(E - E')/$ $4[L^2 k^3 (m-1) EI_0 + E^* A^* b/4]$ $[L^2 k^3 (m-1) E' I_0 + E^* A^* b/4]\}/\mathrm{d}x_P^2$
Tie beam damaged	$225I_0 f A^* E (E^{*\prime} - E^*)(L - x_P)$ $(L + x_P)(x_P n + L - x_P)/2L^4 (8f^2 E^* A^* + 15EI_0)$ $(8f^2 E^{*\prime} A^* + 15EI_0)$	$d^2\{aEA^* L^2 k^3 I_0 (m-1)(E^* - E')/$ $4[L^2 k^3 (m-1) EI_0 + E^* A^* b/4]$ $[L^2 k^3 (m-1) EI_0 + E^{*\prime} A^* b/4]\}/\mathrm{d}x_P^2$

Note. $a = \{f\{[(k+2n-2)L + \mathrm{k}x_p(n-1)]L^2 e^{-\mathrm{k}x_p/L} + L^2 e^{\mathrm{k}x_p/L}\ [(k-2n+2)L + \mathrm{k}x_p(n-1)] - L^2 e^{-k}[\mathrm{kL} + x_p(n-1)(k+2)] - [\mathrm{kL} + x_p(n-1)(k-2)]L^2 e^k + k^3 m(L - x_p)(L + x_p)(L + \mathrm{n}x_p/3 - x_p/3)\}$, $b = L^2 k^2 f^2 (m-1)(8\mathrm{km}^2 + 8e^{-k}m - 8e^k m - e^{-2k} + e^{2k} + 4k)/2(m^2 - 2m + 1)$.

wherein the cross beams, arch ribs, middle longitudinal beams, and tie beams are made of C50. The elastic modulus of C50 concrete is $3.45e+07$ kN/m^2, the Poisson ratio of C50 concrete is 0.2, the volumetric weight is 25 kN/m^3, and the coefficient of linear expansion of C50 concrete is $1.20e-05$ (1/°C). The elastic modulus of the suspender is $2.05e+08$ kN/m^2, the Poisson ratio of the suspender is 0.3, the volumetric weight is 76.98 kN/m^3, and the coefficient of linear expansion of the suspender is $1.20e-05$ (1/°C). The bridge deck is made of C40. The elastic modulus of C40 is $3.25e+07$ kN/m^2 and the Poisson ratio of C40 concrete is 0.2. The volumetric weight is 25 kN/m^3, and the coefficient of linear expansion of the suspender is $1.0e-05$ (1/°C). The elastic modulus of wind brace is $2.06e+08$ kN/m^2, the Poisson ratio of the wind brace is 0.3, the volumetric weight is 76.98 kN/m^3, and the coefficient of linear expansion of wind brace is 1.20e − 05 (1/°C). With a total of 121 loading steps with a loading length of 0.5 m, a quasistatic moving concentrated force is applied to this loading model, as shown in Figure 8.

3.2.1. Analysis of Suspenders' Damage Identification. The preset damage conditions (1–6) of bridge suspenders are listed in Table 6, and the damage position numbers of bridge suspenders are shown in Figure 9. A measuring location is set on unit 25# near the arch foot of the bridge tie beam.

From Figures 10(a)–10(c), it can be seen that peaks corresponding to load steps 31#, 61#, and 91# appear on the ETILDC curves, and when load steps 31#, 61#, and 91# are performed on the bridge deck, damage at the 3#, 6#, and 9# suspenders are located, respectively. With comparisons among curves presented in Figures 10(a) and 10(d), curves presented in Figures 10(b) and 10(e), and curves presented in Figures 10(c) and 10(f), it can be seen that when a pair of suspenders on a same cross beam have the same damage extent, the damaged suspender near the measuring location presents large peak values on ETILDC curves than that damaged suspender far away from the measuring location, showing great effectiveness in

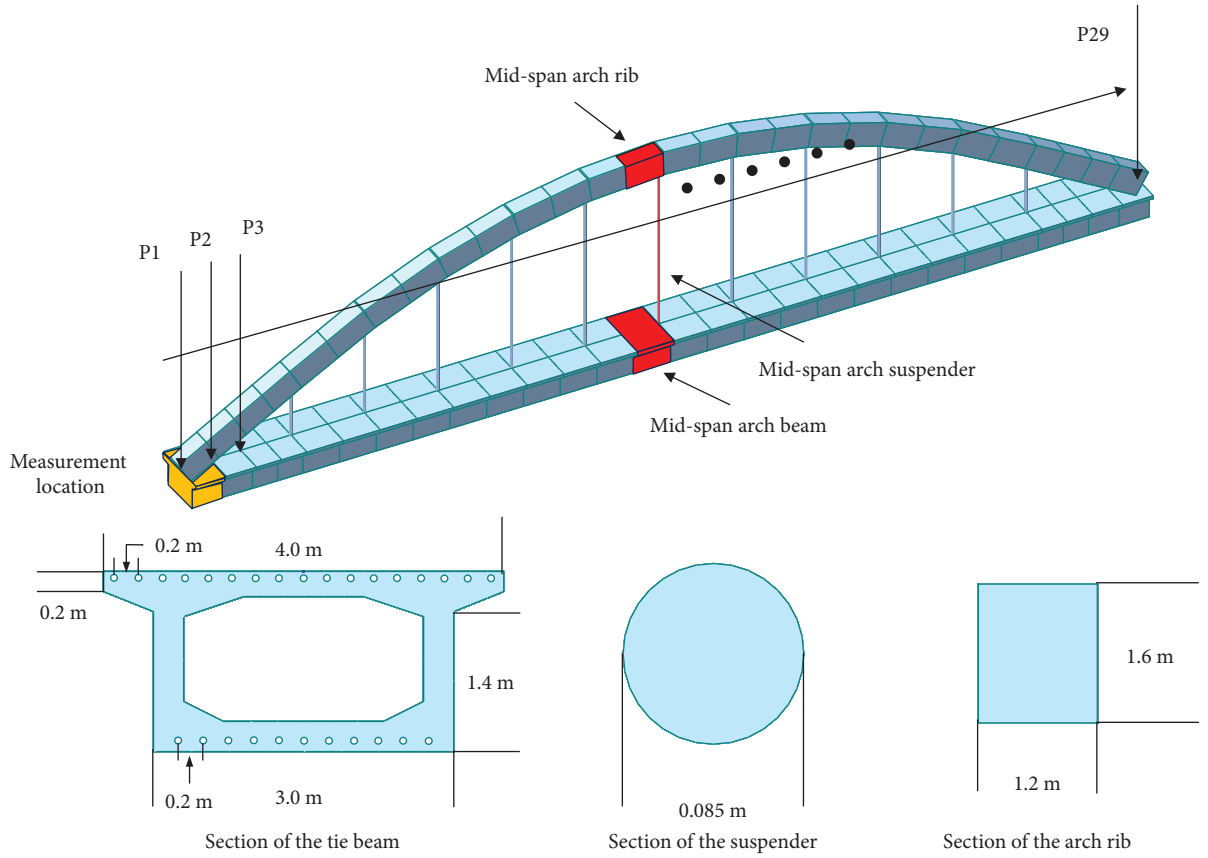

Figure 5: Schematic diagram of quasistatic loading of planar tied-arch structure.

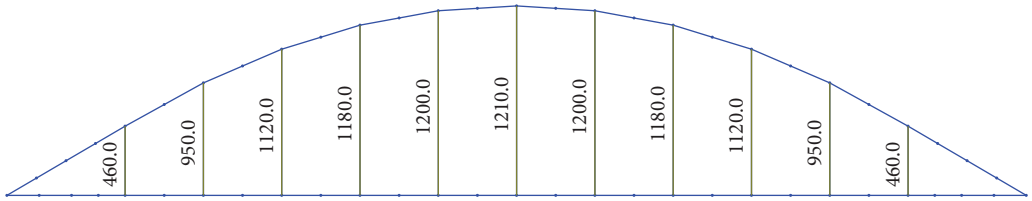

Figure 6: Initial tension of suspenders (unit: kN).

Table 5: Damage conditions of planar tied-arch structure.

Loading methods	Damage location	Damage extent (%)	Result identification
Quasistatic-influenced line loading of the tie beam	Midspan arch beam	10, 30, 50	Figure 7(a)
	Midspan arch rib	10, 30, 50	Figure 7(b)
	Midspan suspender	10, 30, 50	Figure 7(c)

damage identification. This result shows that the ETILDC index presents high accuracy in locating the damage of the suspenders of arch bridges.

3.2.2. Analysis of Arch Ribs' Damage Identification. The preset damage conditions (7–12) of arch ribs are listed in Table 7.

From Figure 11, it can be seen that peak values of ETILDC curves occur between load steps, indicating damaged arch ribs on the corresponding load sections in the FE model. Under work condition 7, the maximum damage peak value among ETILDC curves is close to 2.5E−5 with a damage condition of 50%, while under work condition 8, the maximum damage peak value is only close to 2.5E−6. Therefore, it indicates that if arch ribs on both sides of a tied-arch bridge are damaged at the same position to the same extent, ETILDC is more effective in identifying the damage of those arch ribs on the same side of the bridge with the measuring location. A comparison of curves presented in Figures 11(e) and 11(f) shows that ETILDC is more effective in identifying the damage of arch ribs on the same side of the bridge with the

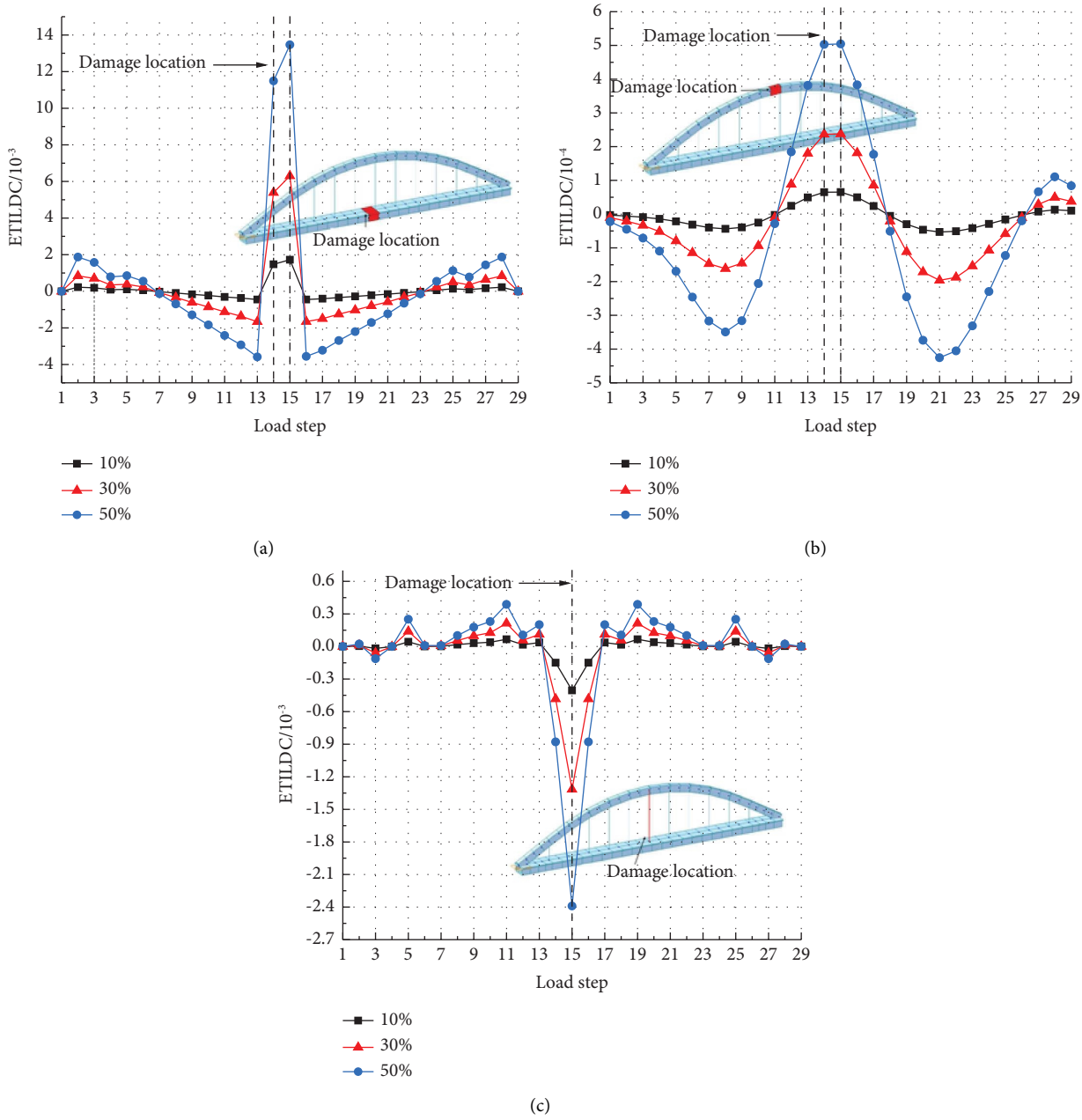

Figure 7: ETILDC damage identification curves of planar tied-arch structure. (a) ETILDC curve of the midspan arch beam. (b) ETILDC curve of the midspan arch rib. (c) ETILDC curve of the midspan arch suspender.

measuring location. A comparison of curves presented in Figures 11(a), 11(c), and 11(e) shows that under the same damage extent of arch ribs, ETILDC will exhibit the greatest effectiveness in identifying the damage of arch ribs at the midspan position. Under an arch rib damage extent of 50%, peak values of ETILDC curves at 1/2, 1/4, and 3/4 bridge spans are $2.44246E-5$, $1.46345E-5$, and $9.29704E-6$, respectively. Besides the fact that ETILDC is most effective in locating the damage of arch ribs at the midspan arch units, there is a negative correlation between the distance between measuring location and damage location and the effectiveness of ETILDC in locating damage. Therefore, the results of this research can be complemented with the addition of more measuring locations. Under the same work conditions, there is a positive correlation between the damage identification effectiveness of the ETILDC index and the damage extent of arch ribs with the same damage location.

3.2.3. Indices of Noise-Immunity Verification. Test or environmental noise may cause deviations between real data and measured data. Therefore, noise is introduced in this paper to verify the immunity of ETILD. Under work condition 1 and with a 10% damage extent applied to the 3# suspender, noise with a 5% level is introduced to the influence line to simulate the noise situation of actual

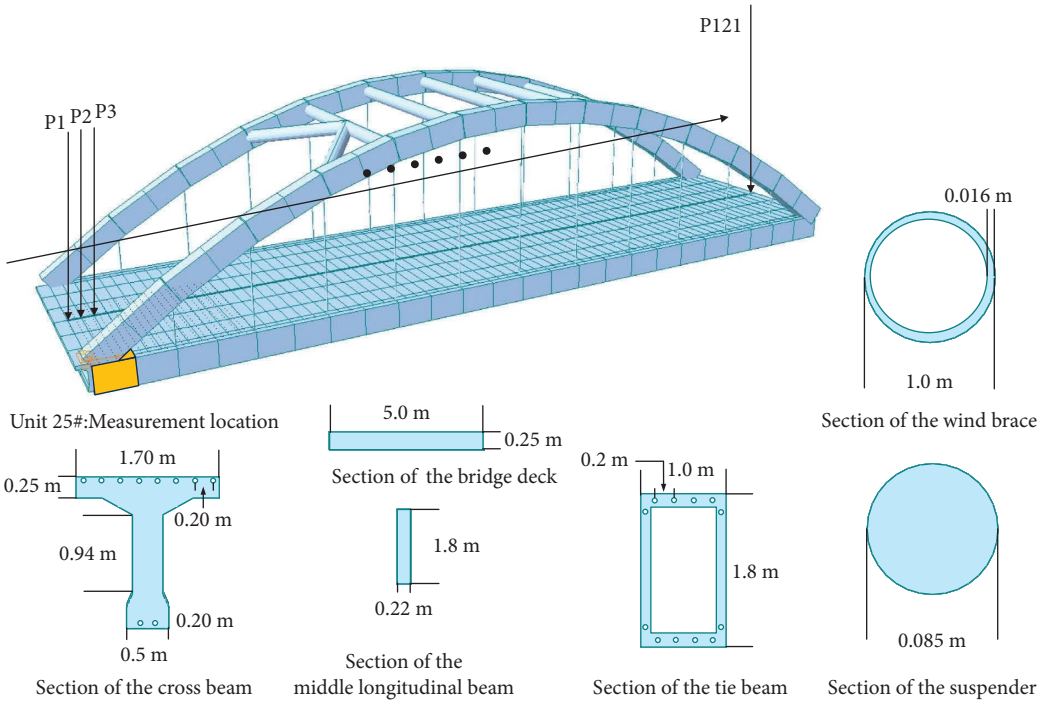

Figure 8: Quasistatic loading scheme of the tied-arch bridge.

Table 6: Damage conditions of suspenders of the tied-arch bridge.

Damage conditions	Measuring location	Damage location	Damage extent (%)	Result
Work condition 1	Unit 25#	Suspender 3#	10, 30, 50	Figure 10(a)
Work condition 2	Unit 25#	Suspender 6#	10, 30, 50	Figure 10(b)
Work condition 3	Unit 25#	Suspender 9#	10, 30, 50	Figure 10(c)
Work condition 4	Unit 25#	Suspender 14#	10, 30, 50	Figure 10(d)
Work condition 5	Unit 25#	Suspender 17#	10, 30, 50	Figure 10(e)
Work condition 6	Unit 25#	Suspender 20#	10, 30, 50	Figure 10(f)

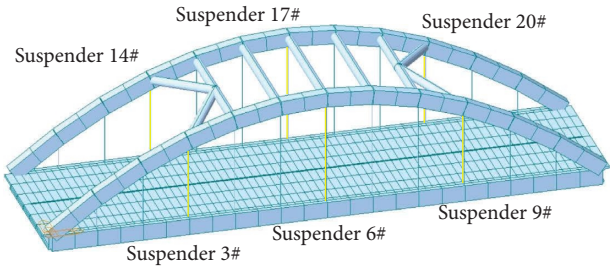

Figure 9: Damage position numbers of suspenders.

measurement. Also, the work condition with noise is set as work condition 13, with the following noise introduction equation:

$$T_i^N = T_i \cdot [1 + \mu \cdot \mathrm{RAND}(-1, 1)], \tag{24}$$

where T_i^N represents the thrust data containing noise under the i loading step; T_i is the thrust data without noise under the i loading step; $\mathrm{RAND}(-1, 1)$ is the standard normal distribution of random numbers; and μ is the noise extent level.

As can be seen from Figure 12, the ETILD curve with noise presents a generally consistent pattern with that pattern of the ETILD curve without noise. In order to further investigate the noise-immunity performance of ETIL, grey relation analysis (GRA) [29] was performed in this research to evaluate the noise immunity of damage identification indicators. Based on cybernetics, grey correlation analysis applies a method of multifactor statistical analysis [30]. This method uses colors to represent how much information is known about a system, with white representing sufficient information, black representing a system whose structure is

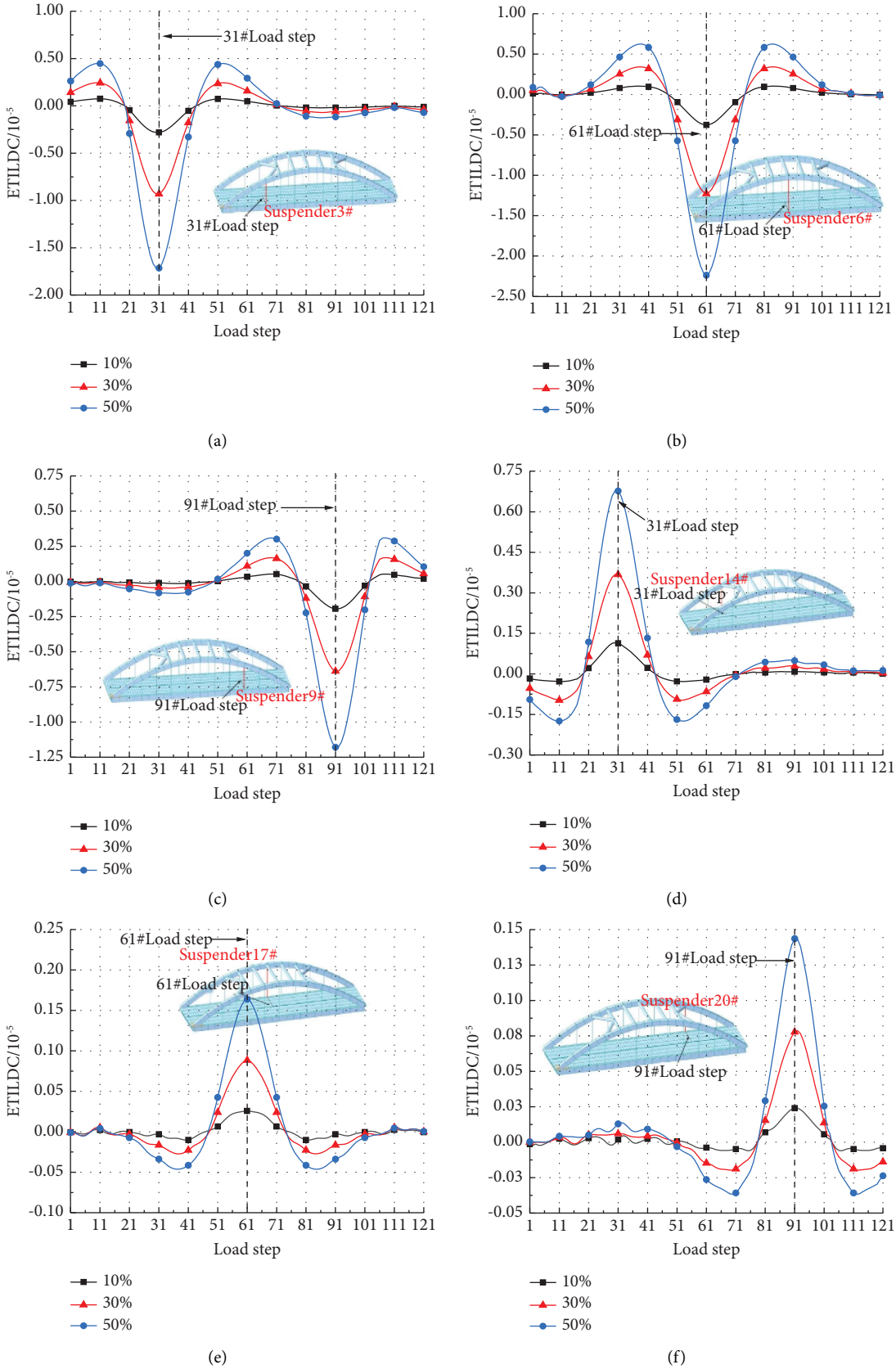

FIGURE 10: Damage identification results of suspenders. (a) Work condition 1. (b) Work condition 2. (c) Work condition 3. (d) Work condition 4. (e) Work condition 5. (f) Work condition 6.

Table 7: Damage conditions of arch ribs of the tied-arch bridge.

Damage conditions	Measuring point	Damage location	Damage extent (%)	Result
Work condition 7	Unit 25#	Unit 7#	10, 20, 30, 40, 50	Figure 11(a)
Work condition 8	Unit 25#	Unit 19#	10, 20, 30, 40, 50	Figure 11(b)
Work condition 9	Unit 25#	Unit 9#	10, 20, 30, 40, 50	Figure 11(c)
Work condition 10	Unit 25#	Unit 22#	10, 20, 30, 40, 50	Figure 11(d)
Work condition 11	Unit 25#	Unit 502#	10, 20, 30, 40, 50	Figure 11(e)
Work condition 12	Unit 25#	Unit 514#	10, 20, 30, 40, 50	Figure 11(f)

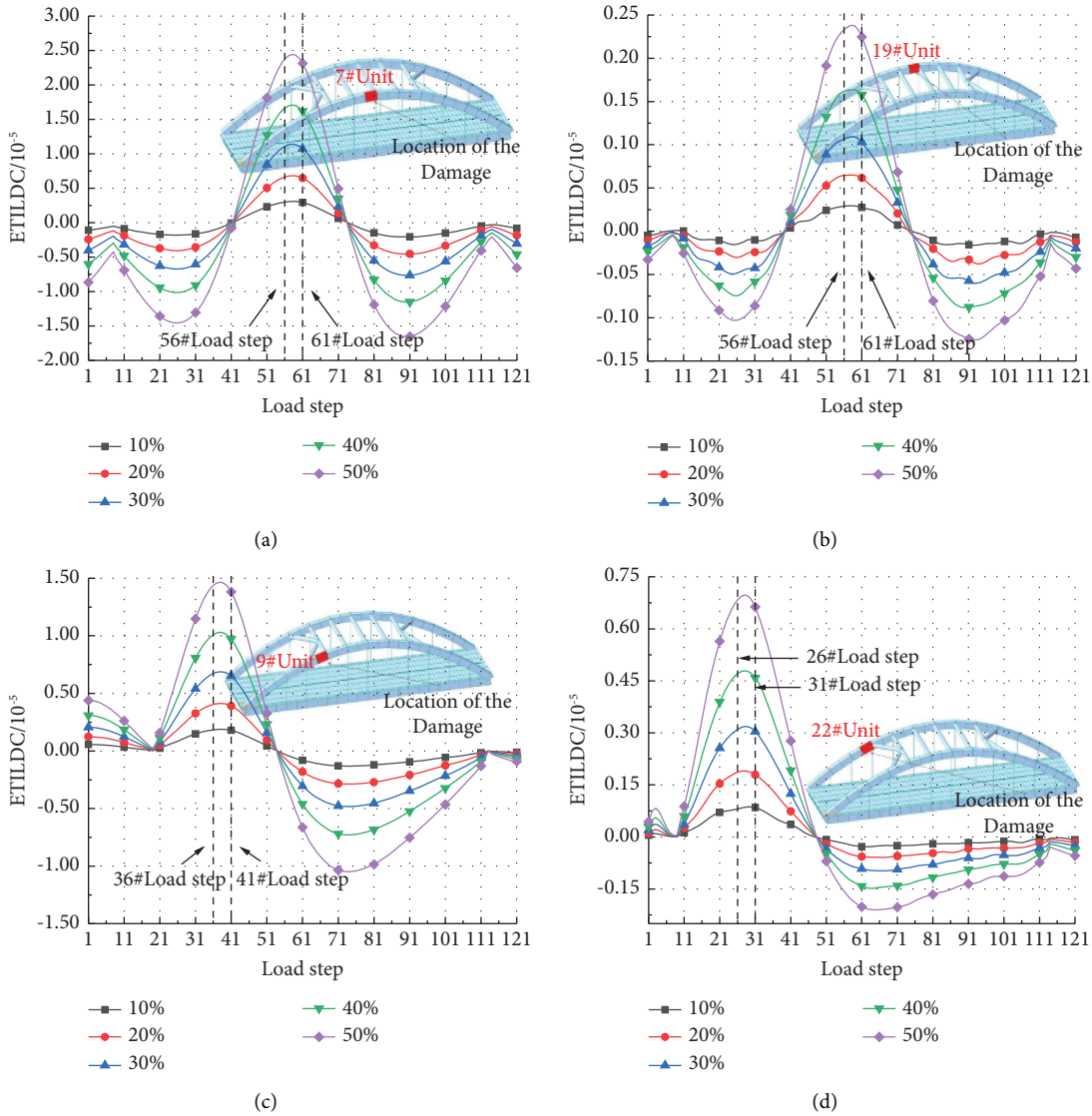

Figure 11: Continued.

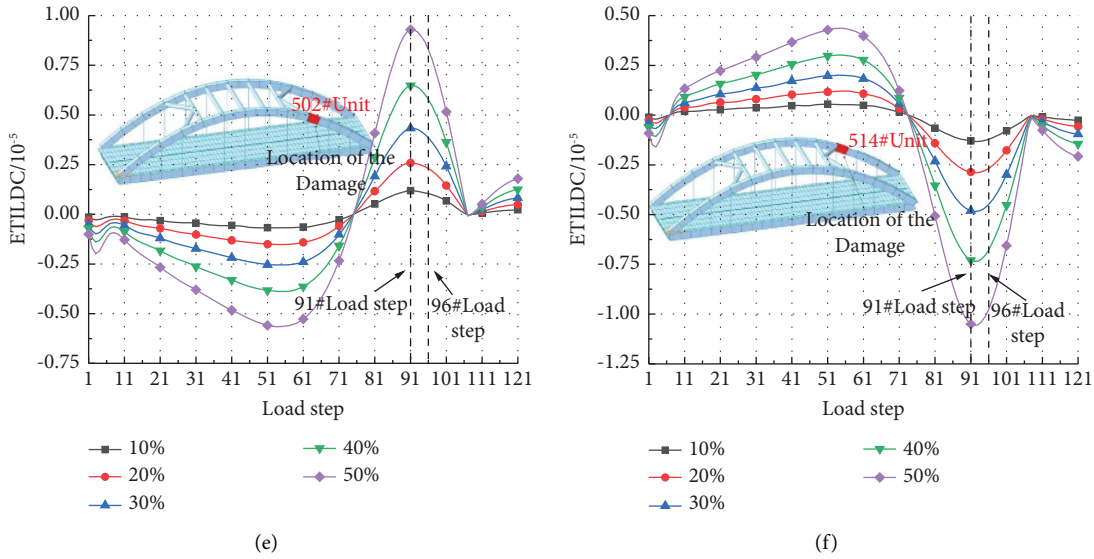

Figure 11: Arch rib damage identification results. (a) Work condition 7. (b) Work condition 8. (c) Work condition 9. (d) Work condition 10. (e) Work condition 11. (f) Work condition 12.

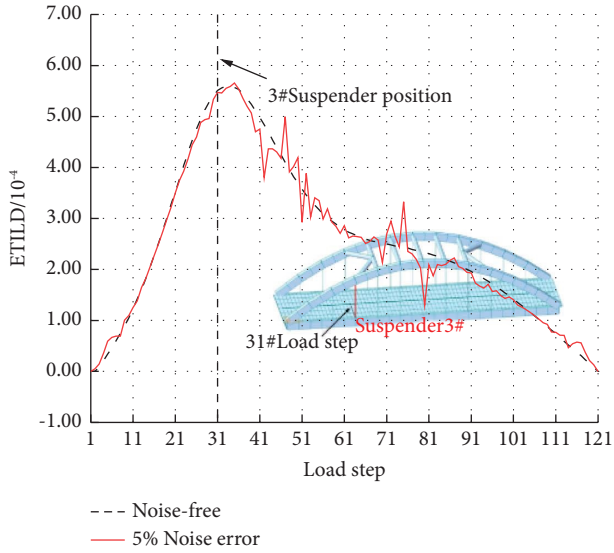

Figure 12: Noise influence on ETILD.

not clear, and grey representing the information in between; that is, only a part of the system is understood [31]. In this grey system, it is crucial to determine the parent sequence, conduct dimensionless processing of data through the mean value, and calculate the grey correlation coefficient through the following equation:

$$\xi_i(k) = \frac{\min_i \min_k |y(k) - x_i(k)| + \rho \cdot \max_i \max_k |y(k) - x_i(k)|}{|y(k) - x_i(k)| + \rho \cdot \max_i \max_k |y(k) - x_i(k)|}, \tag{25}$$

where $\xi_i(k)$ is the correlation coefficient of x_i with $y(k)$ at point k; $|y(k) - x_i(k)|$ is the absolute difference between y and x_i at point k; $\min_i \min_k |y(k) - x_i(k)|$ is the minimum absolute value of the second-order difference between y series and x_i series at k point; $\max_i \max_k |y(k) - x_i(k)|$ is the maximum absolute value of the second-order difference between y series and x_i series at k point; and ρ is the grey resolution coefficient, which ranges from 0 to 1, with a general value of 0.5. Meanwhile, the correlation degree r_i between x_i and $y(k)$ can be obtained through the

substituting of the correlation coefficient of each character into the following equation:

$$r_i = \frac{1}{n}\prod_{k=1}^{n}\xi_i(k). \tag{26}$$

The grey correlation coefficient is calculated in this research with work condition 13 after the introduction of noise retaken as a sample. The grey correlation coefficient can reflect the correlation degrees of data, and with the size of this coefficient, the correlation degree between noiseless data and noise data can be investigated. Through the calculation in this research, it can be seen that the grey correlation coefficients with and without noise obtained the values of 0.6365 and 0.7173, respectively. Compared with the error result of the thrust-influenced line without noise, the error result of the thrust-influenced line with noise is 11.26%, indicating that the ETIL index has good noise immunity in identifying the damage of tied-arch bridges.

4. Thrust-Influenced Line Recognition Based on Variational Mode Decomposition

VMD (variational mode decomposition) is a signal-processing method with adaptive model variation [32]. The adaptive function of the VMD method is to determine the number of mode decomposition of time series according to the actual situation. The optimal solution of variational modes can be searched with the iterative method [33, 34], and the time-domain signal can be decomposed into K finite bandwidths of IMF ranging from high frequency to low frequency. It is assumed that IMF with limited bandwidths is disturbed around their respective central frequencies, and K modes can be iteratively searched. This research set a constraint condition that a combination of all modes makes the original signal [35, 36], and all the models have a minimized combination of estimated bandwidths. The numerical model is expressed in the following equation:

$$\begin{cases} \min\limits_{\{u_i\},\{\omega_i\}} \left\{ \sum\limits_{k=1}^{K} \left\| \partial_t \left[\left(\delta(t) + \dfrac{j}{\pi t} \right) \times u_k(t) \right] e^{-j\omega_k t} \right\|_2^2 \right\}, \\ \text{s.t.} f(t) = \sum\limits_{k=1}^{K} u_k(t). \end{cases} \tag{27}$$

To solve the optimal problem of constrained variation, the quadratic penalty factor α and the alternate multiplication operator $\lambda(t)$ are introduced to transform (27) into an equation of unconstrained variation. The unconstrained Lagrange function is presented in the following equation:

$$L(\{u_i\},\{\omega_i\},\lambda) = \alpha \sum_{i=1}^{K} \left\| \partial_t \left[\left(\delta(t) + \frac{j}{\pi t} \right) \times u_i(t) \right] e^{-j\omega_i t} \right\|_2^2 + \left\| f(t) - \sum_{i=1}^{K} u_i(t) \right\|_2^2 + \left\langle \lambda(t), f(t) - \sum_{i=1}^{K} u_i(t) \right\rangle. \tag{28}$$

The "saddle point" in (28) is obtained through the use of the alternating multiplication operator, with u_k^{n+1}, ω_k^{n+1}, and λ_k^{n+1} iteratively updated. The update formulas are presented in equations (29)–(31).

$$\hat{u}_k^{n+1}(\omega) = \frac{\hat{f}(\omega) - \sum_{i<k} \hat{u}_i^{n+1}(\omega) - \sum_{i<k} \hat{u}_i^{n}(\omega) + \left(\hat{\lambda}^{n}(\omega)/2 \right)}{1 + 2\alpha(\omega - \omega_k^n)^2}, \tag{29}$$

$$\omega_k^{n+1} = \frac{\int_0^\infty \omega \left| \hat{u}_k^{n+1}(\omega) \right|^2 d\omega}{\int_0^\infty \left| \hat{u}_k^{n+1}(\omega) \right|^2 d\omega}, \tag{30}$$

$$\hat{\lambda}^{n+1}(\omega) = \hat{\lambda}^{n}(\omega) + \tau \left[\hat{f}(\omega) - \sum_{k=1}^{K} \hat{u}_k^{n+1}(\omega) \right], \tag{31}$$

where $\wedge$ represents the Fourier transformation and τ represents the time step.

With $\{w_k^l\}$, $\{u_k^l\}$, λ^1, and n initialized and u_k, ε, and λ iteratively updated until the allowable error ε is satisfied, decomposition is stopped and IMF components are finally put as the output (the number of IMF is K). The allowable error criterion is expressed in the following equation:

$$\sum_{k=1}^{K} \frac{\left\| \hat{u}_k^{n+1}(\omega) - \hat{u}_k^{n}(\omega) \right\|_2^2}{\left\| \hat{u}_k^{n}(\omega) \right\|} < \varepsilon. \tag{32}$$

Numerical simulation was performed based on the condition of the original ETIL with measured dynamic disturbance in a 30% damage state in work condition 1. VMD is used to eliminate dynamic components in the numerical simulation. Then, the quasistatic time-history response of the bridge can be obtained, as shown in Figure 13.

It can be seen from Figure 13(a) that with the VMD process method, dynamic components in the thrust response under the loading of the moving vehicle can be effectively eliminated, with a smooth quasistatic thrust influence curve obtained. Figure 13(b) shows that VMD processing will reduce the peak value of the thrust influence curve. Therefore, the quasistatic-influenced line after VMD processing has a smaller shape than the static thrust-influenced line of the structure.

5. Practical Process for Tied-Arch Bridge Damage Identification

Axial force cannot be measured directly. However, in practical engineering, it can be calculated through the measuring of strain on the arch section. In the test of

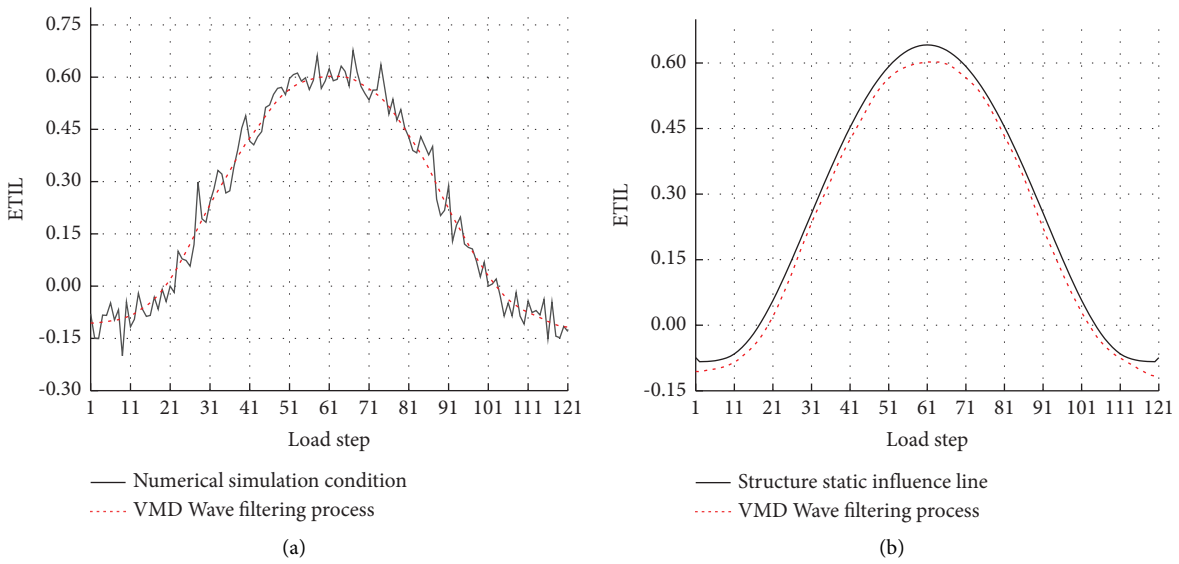

Figure 13: Thrust influences line identification of VMD. (a) Processed by VMD. (b) Data comparison.

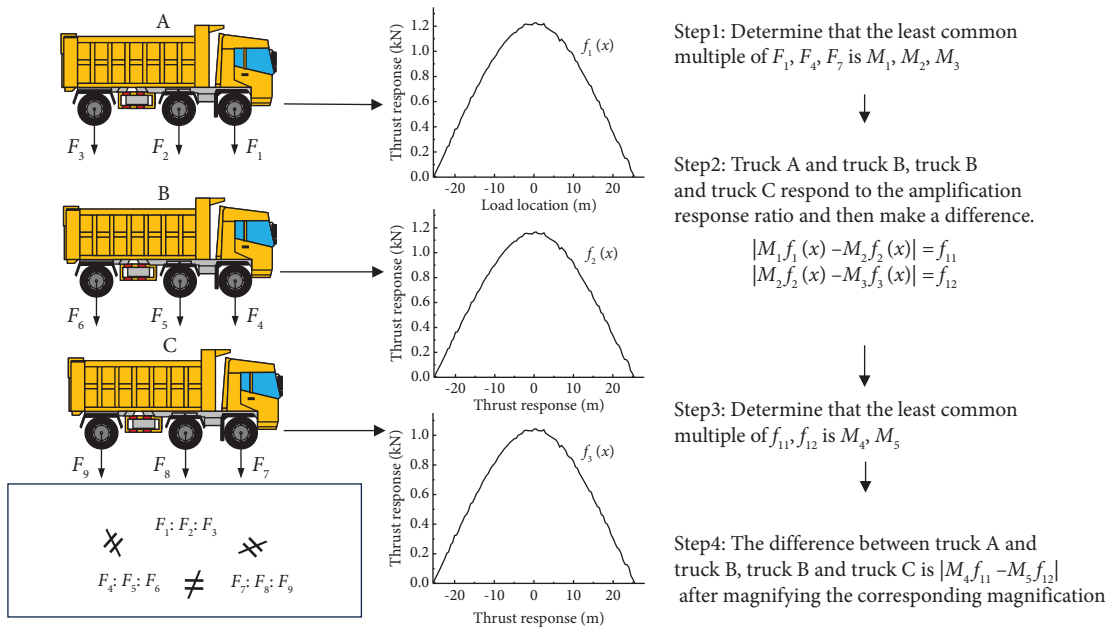

Figure 14: Practical operation process.

influence lines of tied-arch bridges, it is difficult to simulate the unit concentrated forces of influence lines through the application of single-axis-concentrated load. It is an important method to research the damage of bridges by the moving load and dynamic response analysis [37]. Therefore, this paper has proposed a three-step loading process based on moving load reduction and this process can be used for the rapid diagnosis of bridge damage under short traffic interruption [38], as shown in Figure 14.

(1) Three three-axle vehicles with the same wheelbase and different front and rear axle weight ratios are selected as loading tools. The front and rear axles of each vehicle can exert different amounts of concentrated forces at corresponding positions. In the process of loading, concentrated forces should be efficiently applied to the tied-arch bridge to ensure the stability and effectiveness of the structural response measurement.

(2) The three vehicles are, respectively, idle mobile loading on the tied-arch bridge deck to load the tied-arch bridge. The virtual loading of the tied-arch bridge is conducted repeatedly three times at the same position, which can be achieved by controlling the speeds of loading vehicles and collecting those three thrust response data at the same time.

(3) The minimum common multiples M_1, M_2, and M_3 of front axle equivalent-concentrated forces F_1, F_4,

and F_7 of those three vehicles are calculated, and the concentrated forces $|M_1F_1 - M_2F_4|$ and $|M_1F_1 - M_2F_4|$ can be obtained through the difference after the corresponding magnification. Similarly, the minimum common multiple M_4 and M_5 of virtual loading-concentrated force is determined, and the equivalent loading concentrated force, $|M_4|M_1F_1 - M_2F_4| - M_5|M_2F_4 - M_3F_7||$, can be obtained through the difference after the corresponding magnification. The measurement of thrust-influenced line data $f_1(x)$, $f_2(x)$, and $f_3(x)$ is performed repeatedly for three times and then these measured data are amplified with multiples of M_1, M_2, and M_3. After that, the thrust-influenced line $|M_4|M_1f_1(x) - M_2f_2(x)| - M_5|M_2f_2(x) - M_3f_3(x)||$ under the loading of concentrated force can be obtained and used to diagnose the damage of the tied-arch bridge.

6. Conclusions

(1) In this research, it is observed that with the decrease of rise-span ratio, axial deformation has a gradually increased influence on the arch structures. Under a rise-span ratio greater than 1/7, the calculation error of the derived practical analytical solution for ETIL is less than 9.57%, indicating that this solution can effectively calculate and analyze the damage of arch structure with a tie beam under a rise-span ratio ranging from 1/4 to 1/5.

(2) The analytical difference curvature of ETIL can be effectively used in the damage identification of planar tied-arch structures. Tie beams, suspenders, and arch ribs are the main stressed components of arch bridges suitable for damage identification. In actual measuring scenarios of ETIL at the arch feet, measuring locations along influence lines can be arranged near those tie beams that are close to the arch feet units.

(3) It has been proved that the curvature method established based on the differential effects of ETIL is effective in identifying damage in suspenders and arch ribs at different positions of tied-arch bridges. This method is particularly helpful in assessing the health status of bridge suspenders. Qualitative analysis shows that the identification of damage extents of different bridge components relies on the index amplitude with good noise immunity by grey correlation analysis.

(4) In this research, thrust-influenced line recognition based on VMD (variational mode decomposition) is introduced and a practical approach for assessing the health status of arch bridges based on quasistatic impact lines was proposed; this approach is suitable for efficiently testing the impact lines of crucial components of arch bridges under the static loading of three-axle vehicles. With a combination of existing bridge monitoring methods, the identification method of arch bridge damage proposed in this paper has the prospect of facilitating routine health assessment of in-service arch bridges in the future.

(5) This research is helpful in developing methods for damage diagnosis and load-bearing capacity assessment of tied-arch bridges. It provides a new idea for structural health monitoring of tied-arch bridges. The influence line has the function of reflecting the structural characteristics. The damage identification and diagnosis method of the tied-arch bridge based on ETIL is high efficiency, so the health detection and monitoring based on the equivalent thrust-influenced line has a good development prospect.

Data Availability

The datasets used to support the findings of this study are available from the corresponding author on reasonable request.

Conflicts of Interest

The authors declare that they have no conflicts of interest.

Authors' Contributions

Y. Zhou designed the research, developed the approach, performed the experiment, and analyzed the data. M. Li designed the research, analyzed the data, and wrote and revised the manuscript. Y.D. Shi, S.K. Di, and X.Z. Shi analyzed the data and revised the manuscript. All the authors have reviewed the manuscript.

Acknowledgments

The authors would like to acknowledge the financial support received from the Natural Science Foundation Youth Project of Anhui Province (no. 2008085QE247), the University Outstanding Top Talent Cultivation Project of Anhui Province (no. gxgnfx2022021), the University Scientific Research Major Project of Anhui Province (no. 2022AH050248), the Foundation of National and Local Joint Engineering Laboratory of Building Health Monitoring and Disaster Prevention Technology (no. GG22KF002), and the Construction Technology Project Plan of Gansu Province (no. JK2023-03).

References

[1] W. Huang, M. S. Pei, X. D. Liu, and Y. Wei, "Design and construction of super-long span bridges in China: review and future perspectives," *Frontiers of Structural and Civil Engineering*, vol. 14, no. 4, pp. 803–838, 2020.

[2] B. C. Chen, "State-of-The-Art of the development of arch bridges in China," in *Proceedings of the 4th International Conference on New Dimensions in Bridges. Flyovers, Overpasses and Elevated Structures*, pp. 13–24, China, January 2017.

[3] B. H. Fan, J. Z. Su, and B. C. Chen, "Condition evaluation for through and half-through arch bridges considering robustness of suspended deck systems," *Advances in Structural Engineering*, vol. 24, no. 5, pp. 962–976, 2021.

[4] P. Lonetti, A. Pascuzzo, and A. Davanzo, "Dynamic behavior of tied-arch bridges under the action of moving loads," *Mathematical Problems in Engineering*, 2016.

[5] J. P. Sun, J. B. Li, Y. B. Jiang, X. G. Ma, Z. H. Tan, and G. L. Zhufu, "Key construction technology and monitoring of long-span steel box tied arch bridge," *International Journal of Steel Structures*, vol. 23, no. 1, pp. 191–207, 2023.

[6] Y. Yang, B. Q. Lin, and W. Zhang, "Experimental and numerical investigation of an arch–beam joint for an arch bridge," *Archives of Civil and Mechanical Engineering*, vol. 23, no. 2, p. 101, 2023.

[7] C. D. Tetougueni, P. Zampieri, and C. Pellegrino, "Lateral stability of network arch bridges," *Structural Integrity*, vol. 11, pp. 358–365, 2019.

[8] P. Zampieri, C. D. Tetougueni, E. Maiorana, and C. Pellegrino, "Post-buckling of network arch bridges subjected to vertical loads," *Structure and Infrastructure Engineering*, vol. 17, no. 7, pp. 941–959, 2021.

[9] B. H. Fan, S. G. Wang, and B. C. Chen, "Dynamic effect of tie-bar failure on through tied arch bridge," *Journal of Performance of Constructed Facilities*, vol. 34, no. 5, 2020.

[10] Y. Zhou, M. Li, Y. Shi, C. Xu, D. Zhang, and M. Zhou, "Research on damage identification of arch bridges based on deflection influence line analytical theory," *Buildings*, vol. 14, no. 1, p. 6, 2023.

[11] M. Civera, V. Mugnaini, and L. Zanotti Fragonara, "Machine learning-based automatic operational modal analysis: a structural health monitoring application to masonry arch bridges," *Structural Control and Health Monitoring*, vol. 29, no. 10, 2022.

[12] L. F. Ge, K. Y. Koo, M. M. Wang, J. Brownjohn, and D. H. Dan, "Bridge damage detection using precise vision-based displacement influence lines and weigh-in-motion devices: experimental validation," *Engineering Structures*, vol. 288, no. 1, 2023.

[13] P. Lonetti, A. Pascuzzo, and S. Aiello, "Instability design analysis in tied-arch bridges," *Mechanics of Advanced Materials and Structures*, vol. 26, no. 8, pp. 716–726, 2019.

[14] B. Bozyigit and S. Acikgoz, "Determination of free vibration properties of masonry arch bridges using the dynamic stiffness method," *Engineering Structures*, vol. 250, no. 1, 2022.

[15] Z. W. Chen, L. Zhao, J. Zhang, Q. L. Cai, J. Li, and S. Y. Zhu, "Damage quantification of beam structures using deflection influence line changes and sparse regularization," *Advances in Structural Engineering*, vol. 24, no. 9, pp. 1997–2010, 2021.

[16] C. C. Fan, Y. X. Zheng, B. L. Wang, Y. Zhou, and M. Sun, "Damage identification method for tied arch bridge suspender based on quasi-static displacement influence line," *Mechanical Systems and Signal Processing*, vol. 200, no. 1, 2023.

[17] M. Breccolotti and M. Natalicchi, "Bridge damage detection through combined quasi-static influence lines and weigh-in-motion devices," *International Journal of Civil Engineering*, vol. 20, no. 5, pp. 487–500, 2021.

[18] S. Zhu, Z. W. Chen, Q. L. Cai, Y. Lei, and B. Chen, "Locate damage in long-span bridges based on stress influence lines and information fusion technique," *Advances in Structural Engineering*, vol. 17, no. 8, pp. 1089–1102, 2014.

[19] B. H. Fan, S. G. Wang, and B. C. Chen, "Robustness assessment framework for through tied-arch bridge considering tie-bar failure," *Journal of Bridge Engineering*, vol. 27, no. 5, pp. 1–15, 2022.

[20] Y. F. Duan, Q. Y. Chen, H. M. Zhang, C. B. Yun, S. K. Wu, and Q. Zhu, "CNN-based damage identification method of tied-arch bridge using spatial-spectral information," *Smart Structures and Systems*, vol. 23, no. 5, pp. 507–520, 2019.

[21] Q. Feng, P. Wei, J. B. Lou, J. B. Cai, and R. Q. Xu, "Analytical solution for quick decision of tied–arch bridge parameters at early-design stage based on Hellinger–Reissner variational method," *Structures*, vol. 44, pp. 1443–1453, 2022.

[22] B. H. Fan, S. G. Wang, B. C. Chen, P. F. Chao, and Q. Sun, "Robustness-based condition evaluation framework for through tied-arch bridge," *Journal of Performance of Constructed Facilities*, vol. 37, no. 2, 2023.

[23] Y. Zhou, S. K. Di, C. S. Xiang, W. R. Li, and L. X. Wang, "Damage identification in simply supported bridge based on rotational-angle influence lines method," *Transactions of Tianjin University*, vol. 24, no. 6, pp. 587–601, 2018.

[24] M. Q. Gu and S. F. Shi, *Highway Bridge and Culvert Design Manual. Arch Bridge (Book One)*, Book One, Eden Terrace, Auckland.

[25] Y. Q. Long, *Structural Mechanics*, Higher Education Press, Beijing, China, 1994.

[26] B. Bozyigit and S. Acikgoz, "Dynamic amplification in masonry arch railway bridges," *Structures*, vol. 45, pp. 1717–1728, 2022.

[27] B. Bozyigit, Y. Yesilce, and M. A. Wahab, "Transfer matrix formulations and single variable shear deformation theory for crack detection in beam-like structures," *Structural Engineering & Mechanics*, vol. 73, no. 2, pp. 109–121, 2020.

[28] B. Bozyigit, Y. Yesilce, and M. A. Wahab, "Free vibration and harmonic response of cracked frames using a single variable shear deformation theory," *Structural Engineering & Mechanics*, vol. 74, no. 1, pp. 33–54, 2020.

[29] L. H. Yin, Y. Wang, T. J. Yu, H. T. Zhang, H. M. Wang, and D. Chen, "Study on micromechanisms of macro evaluation indexes for asphalt based on grey relation analysis," *International Journal of Pavement Engineering*, vol. 23, no. 14, pp. 5186–5197, 2022.

[30] H. J. Li, W. Hu, C. B. Li, Y. P. Ding, and Z. G. Xie, "Review on grey relation applied in image sparse representation," *Journal of Grey System*, vol. 31, no. 1, pp. 52–65, 2019.

[31] P. Z. Lu, S. M. Huang, Y. Shen, Y. Wu, and D. G. Li, "Mix design of asphalt plug joint based on response surface method and grey relational analysis," *International Journal of Pavement Engineering*, vol. 24, no. 2, 2022.

[32] M. Mazzeo, D. De Domenico, G. Quaranta, and R. Santoro, "Automatic modal identification of bridges based on free vibration response and variational mode decomposition technique," *Engineering Structures*, vol. 280, no. 1, 2023.

[33] R. C. Zhang, C. F. Gao, S. G. Pan, and R. Shang, "Fusion of GNSS and speedometer based on VMD and its application in bridge deformation monitoring," *Sensors*, vol. 20, no. 3, p. 694, 2020.

[34] J. Z. Xin, Y. Jiang, J. T. Zhou, L. L. Peng, S. Y. Liu, and Q. Z. Tang, "Bridge deformation prediction based on SHM data using improved VMD and conditional KDE," *Engineering Structures*, vol. 261, no. 15, 2022.

[35] X. M. Yang, C. X. Qu, T. H. Yi, H. N. Li, and H. Liu, "Modal analysis of a bridge during high-speed train passages by enhanced variational mode decomposition," *International Journal of Structural Stability and Dynamics*, vol. 20, no. 13, Article ID 2041002, 2020.

[36] J. X. Li, T. H. Yi, C. X. Qu, H. N. Li, and H. Liu, "Adaptive identification of time-varying cable tension based on improved variational mode decomposition," *Journal of Bridge Engineering*, vol. 27, no. 8, 2022.
[37] B. Bozyigit, "Dynamic response of damaged rigid-frame bridges subjected to moving loads using analytical based formulations," *Engineering Computations*, vol. 40, no. 4, pp. 793–822, 2023.
[38] N. B. Wang, W. Shen, C. R. Guo, and H. P. Wan, "Moving load test-based rapid bridge capacity evaluation through actual influence line," *Engineering Structures*, vol. 252, no. 1, 2022.